Journal of Applied Electrochemistry **32**: 1029–1037, 2002.

High-rate electrochemical dissolution of Ni–Cu alloys in nitrate electrolyte

W. HOOGSTEEN[1,*], S. KUINDERSMA[2], B.P. MINKS and A.D. DAVYDOV[3]
[1]*Laboratory for Technology and Materials, Philips Domestic Appliances and Personal Care BV, Oliemolenstraat 5, PO Box 20100, 9200 CA Drachten, The Netherlands*
[2]*Present address: Philips Enabling Technologies Group, Zwaanstraat 1, 5600 JC Eindhoven, The Netherlands*
[3]*Frumkin Institute of Electrochemistry, Russian Academy of Sciences, Leninskii Prospekt 31, Moscow, 117071 Russia*
*(*author for correspondence, e-mail: w.hoogsteen@philips.com)*

Received 28 August 2001; accepted in revised form 19 June 2002

Key words: alloys, current efficiency, flow-channel cell, high-rate electrochemical dissolution, voltammogram

Abstract

High-rate anodic dissolution of nickel, copper, and two alloys Ni30Cu70 and Ni65Cu32 in $NaNO_3$ solution was studied, using a flow-channel electrochemical cell. In all experiments, the initial interelectrode distance was 208 μm and the electrolyte velocity was 15 m s^{-1}. The dependence of the current efficiency and surface brightening on the current density was determined. Voltage transients at various current densities were measured and voltammograms were constructed. Compared to nickel and copper, the alloys showed intermediate behaviour, especially at $j > j_l$. The shape of the voltage transients and the occurrence of surface brightening were more suitable to detect the existence of a limiting current region than voltammograms, especially for Ni. Using the voltammograms and literature data, anodic and cathodic potentials and the voltage drop in the interelectrode gap at a given current density were estimated for $j < j_l$.

List of symbols

A_{fc}	flow-channel cathode surface area
A_{rd}	rotating disc electrode surface area
C_b	bulk concentration
d	width of flow-channel
D	pipe diameter
h	interelectrode gap
D_d	diffusion constant
D_h	hydraulic diameter $2hd/(h+d)$
E_a	anode potential
E_{act}	potential of activation
E_c	cathode potential
E_{el}	sum of anode and cathode potential
E_{ox}	potential of onset of oxygen evolution
F	Faraday constant
i_l	limiting current
j	current density
j_l	limiting current density
j_{cr}	critical current density
L	length of cathode
M_i	molecular weight of component i
n	number of electrons involved in electrochemical reaction
n_i	dissolution valence of component i
Re	Reynolds number (VD_h/v)
Sc	Schmidt number (v/D_d)
Sh	Sherwood number $(i_l D_h/A_{fc}nFC_bD_d)$
t	time
t_p	time to reach peak cell voltage
V	electrolyte velocity in flow-channel
U	cell voltage
U_i	initial cell voltage
$U_{i,ext}$	initial cell voltage obtained by extrapolation
U_{ohm}	Ohmic voltage drop in interelectrode gap
U_p	peak cell voltage
x	distance from leading edge of electrode
x_i	mass fraction of component i
Δm	weight loss

Greek Symbols

η	viscosity
θ	current efficiency
ρ	density
σ	conductivity of electrolyte
v	kinematic viscosity (η/ρ)
ω	rotation rate

1. Introduction

Systematic studies of high-rate electrochemical dissolution have been performed mainly for pure metals [1]. Only in a few cases, have data on the effect of alloy composition on its anodic behaviour during electrochemical machining (ECM) been reported [2]; for example, on the effect of the components in nickel–chromium alloys [3]. Here, we study high-rate electrochemical

dissolution of nickel–copper alloys in comparison with pure copper and nickel in nitrate electrolyte during ECM.

To explain results, both those available from the literature and those obtained here, we use a schematic sketch of the polarization curves for nickel and copper in sodium nitrate (Figure 1) based on experimental results obtained by various authors.

High-rate electrochemical dissolution of copper in nitrates and sulfates during ECM has been studied [4–8]. The current–voltage characteristics of the process involve three main parts (Figure 1). These correspond to active dissolution (ab), the limiting current density, j_l, region (bc) and transpassive dissolution (cd). Active dissolution is restricted by a critical current density j_{cr}, which may be equal to j_l or slightly higher, depending on the experimental conditions. The limiting current may be constant or decrease somewhat with increasing anodic potential (E_a), for transpassive dissolution j increases with E_a. In the region of active dissolution, the surface is etched and the oxidation state of copper in the dissolution product is 2. In the transpassive region, the surface is brightened and flow streaks and, sometimes, pits are observed. In this region, the oxidation state decreases to a value between 1 and 2. The difference between the potentials of dissolving metal in the active and transpassive regions may reach several volts. The limiting current is reached when the solution near the anode becomes saturated with copper nitrate and a deposit forms on the metal surface. The presence of the deposit leads to suppression of etching. The limiting current is connected to mass transfer in the boundary layer and the solubility of copper nitrate, which in turn depends on the concentration of the nitrate electrolyte. Therefore, j_l increases with increase in electrolyte flow rate V (or disc electrode rotation rate ω) and a decrease in electrolyte concentration. The mechanism of transition to transpassivity (over-limiting currents) and metal dissolution in this state is unclear.

The shape of the corresponding chronopotentiometric curves depends on the applied current density. After $j < j_{cr}$ is switched-on, the potential increases stepwise to a value required to maintain the corresponding j of active dissolution and, then, does not vary with time. At $j > j_{cr}$, the potential increases to a certain value in the region of active dissolution, which is maintained for a certain time until the near-electrode concentration of dissolved copper reaches saturation. Then, a stepwise increase in potential to a higher value corresponding to transpassive dissolution is observed.

The high-rate electrochemical dissolution of nickel in nitrate solutions has been reported [9–17]. It was found that dissolution proceeds in the 'transpassive' state. More precisely, high-rate dissolution starts after anodic activation of the passive metal, which is of the pitting type. The specific feature of this case (as compared, for example, with dissolution in chloride electrolyte) is that activation occurs at a potential, E_{act}, more positive than that of the onset of anodic oxygen evolution E_{ox} (Figure 1). In the potential range between the onset of oxygen evolution and anodic activation, the entire current is consumed by water electrolysis with oxygen evolution and the current efficiency for metal dissolution is close to zero. At the onset of anodic activation in the individual pits, dissolution propagates at higher or lower rate, depending on the value by which the anodic potential exceeds the potential of activation onset, throughout the anodic surface. The current efficiency increases, reaching approximately 90% depending on concentration, temperature and electrolyte flow. The anodic polarization curve for nickel in nitrate electrolyte in the so-called transpassive region has two regions 'ef' and 'gi', where the current increases with potential. These regions are separated by a very small [11, 15, 16] limiting current region ('fg', Figure 1). The limiting current is associated with the saturation of the near–electrode layer and formation of a nickel salt film. In the limiting-current region and at higher currents, surface brightening is observed (at lower j, etching is observed).

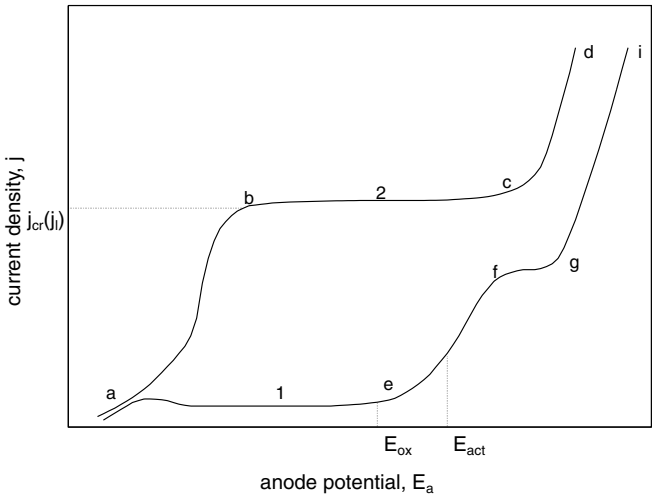

Fig. 1. Scheme of anodic polarization curves for (1) nickel and (2) copper in nitrate electrolyte.

At a certain ratio between current density and electrolyte flow rate, two regions – etching and polishing – with rather sharp boundary between them, may exist simultaneously. The oxidation state of nickel in the high-rate dissolution products is 2.

For the chronoammograms, observations similar to those in the case of copper have been made [11].

No studies of the high-rate dissolution of nickel–copper alloys are available. From results obtained for dissolution at relatively low j in sulfuric acid solutions [18, 19], it may be concluded that at an alloy nickel content of approximately up to 60 wt %, dissolution of the alloys is controlled by the copper component. By contrast, in alkaline solutions, the electrochemical behaviour of Ni–Cu alloys is controlled by the nickel component [20].

2. Experimental procedure

2.1. *Flow-channel cell*

The flow-channel cell design was similar to that of Landolt [21]. The width of the flow channel (d) was 1.0 cm. The length (L) of the bronze cathode was 0.506 cm and its width 0.710 cm. The anode was much larger and aligned with its leading edge exactly parallel to the leading edge of the cathode. In order to guarantee a fully developed velocity profile at the electrodes, the leading edge of each electrode was positioned 3.1 cm downstream from the inlet of the flow channel, which corresponds to 76 hydraulic diameters. The initial interelectrode distance (h) was 208 ± 10 μm.

2.2. *Electrolyte supply*

Technical grade $NaNO_3$ (BASF) was used to prepare solutions with a concentration of about 230 kg m^{-3}. This $NaNO_3$ contained small amounts of impurities (wt %): 0.002 $NaNO_2$, 0.02 Na_2CO_3, 0.09 NaCl, 0.02 Na_2SO_4, 0.026 K, 0.001 Ca, 0.0001 NH_4^+, 0.0003 Fe and 0.000 02 Cu. In addition, it contained about 0.08 wt % anti-caking agent Unipersol-S (a sodium salt of phenyl ethyl naphthalene sulfonic acid). The electrolyte solution was prepared in deionized water (Millipore; conductivity 1.0 μS cm^{-1}) in amounts ranging from 20 to 50×10^{-3} m^3.

A MPA vane pump of type 414/316 CS (Pompe Caster, Vicenza, Italy) was used to circulate the electrolyte. The flow rate was adjusted with a PIV electronics positron-S frequency inverter of type FN351-8/29 (PIV Eldutronik, Bladel, The Netherlands) and fine-tuning was performed with a Philips KS4580 PID controller. The flow rate was measured with a Rosemount magnetic flow tube of type 8711-RRE-15FR4 (Rosemount Inc., USA). To avoid entry of metal hydroxides into the flow-channel a Pall filter block SCY1001-G12 H4Y equipped with a HDCII filter of type MCY1001J200J (Pall, Portsmouth, UK) was placed in the tube between the pump and the flow channel. Mainly Swagelok tubing (reinforced Buna-N rubber) and stainless steel fittings were used in the loop from electrolyte vessel to flow-channel and back to the vessel.

The electrolyte temperature was controlled using a Neslab HX-150 analogue/digital refrigerated recirculator with a centrifugal CP-25 pump. With this unit the temperature could be adjusted from about 10 to 40 °C.

The pH and conductivity (σ) of the electrolyte were measured in a small (about 300 ml) vessel placed immediately behind the flow-channel cell. pH was measured with a Prominent Dulcotest PHEX112 SE electrode using a Prominent Dulcometer pH transmitter/controller of type PHWS 014 F2K2. A Pt100 SE resistance thermometer was used for automatic temperature compensation. To suppress electric noise, a stainless steel bar was placed in the small vessel (sample reference potential). The conductivity was measured with an Omega CDE 3600 electrodeless conductivity sensor using an Omega CDCN-672 conductivity analyser.

2.3. *Power source*

A field effect transistor-controlled current source was used working in a current range from 0 to 50 A and a voltage range of 0–50 V. The slew-rate of the power supply was about 2.5×10^6 A s^{-1}.

2.4. *Data acquisition*

During an ECM experiment, the current, cell voltage (voltage between the electrodes), electrolyte temperature (measured immediately behind the electrodes), pH, conductivity and electrolyte flow rate could be monitored. For data acquisition, an IBM compatible computer was equipped with a BE490 series advanced-transient recorder plug-in cart and TEAM490 software (Bakker Electronics, Dongen, The Netherlands). With this data acquisition system, data could be gathered at up to eight analogous input channels simultaneously. The total amount of samples, which could be stored was 128 000. The maximum sampling frequency was 100 kHz (i.e., if all channels were used, samples could be taken every 10 μs for a period of 160 ms). To avoid common mode problems, differential probes (Ter Mul, Valkenswaard, The Netherlands) were used for measuring cell voltage and current.

2.5. *Mass transfer characteristics*

The mass transfer characteristics of the flow-channel cell were determined using the procedure similar to that described by Landolt [21]. First, the diffusion constant of the redox couple KI/I_2 was measured using a Pt rotating disc electrode. For this purpose, we used Tacussel equipment (a rotating disc electrode), a Wenking Pos 88 potentioscan and a Philips 8141 X–Y recorder. The limiting current (i_l) for the reaction

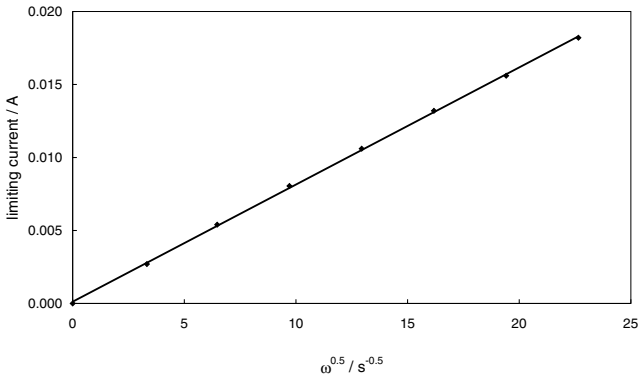

Fig. 2. Limiting current in the iodine–iodide system against square root of the rotation rate of a platinum disc electrode.

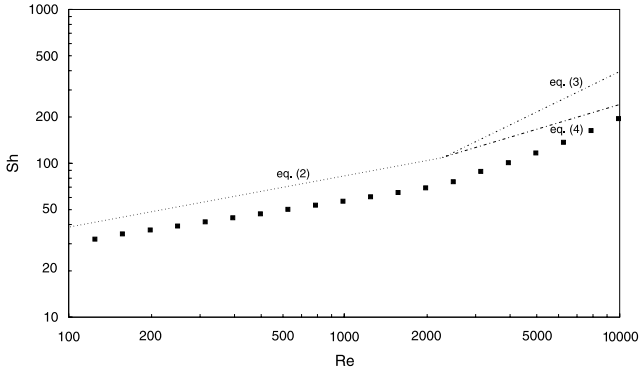

Fig. 3. Sherwood number against Reynolds number characterizing mass transfer conditions in the flow-channel cell: experimental results (filled squares) and curves calculated by Equations 2–4.

$I_3^- + 2e^- \rightarrow 3I^-$ was measured in a solution of 1.0 mol l^{-1} KI and $C_b = 0.01$ mol l^{-1} I_2 at a potential sweep rate of 50 mV s^{-1}. On i_l against $\omega^{1/2}$ coordinates, the obtained dependence yields a straight line (Figure 2) in accordance with the following equation [22]:

$$i_l = 0.62\, nFD_d^{2/3} A_{rd} v^{-1/6} C_b \omega^{1/2} \tag{1}$$

The diffusion coefficient of electroactive species I_3^-, $D_d = 7.5 \times 10^{-6}$ cm^2 s^{-1}, was calculated from the slope of i_l against $\omega^{1/2}$. For calculation of D_d we used $n = 2$, $v = \eta/\rho = 0.008\,26$ cm^2 s^{-1} and $A_{rd} = 0.7854$ cm^2. The viscosity (η) and density (ρ) values were interpolated from data for KI solutions [23]. The value of D_d was somewhat lower than $D_d = 9.17 \times 10^{-6}$ cm^2 s^{-1} from [24].

To compare the mass transfer characteristics of our flow channel with that used by others, the dimensionless Sherwood (*Sh*), Reynolds (*Re*) and Schmidt (*Sc*) numbers were determined at various electrolyte flow rates using the same KI/I_2 solution as used for the rotating disc electrode experiments. The results were compared with (empirical) relationships described in literature [21, 25–30].

The limiting current i_l was determined at a potential of −0.8 V (MSE) as a function of the electrolyte velocity (V). In the calculations of *Re*, *Sh* and *Sc*, the hydraulic diameter (D_h) and surface area of the cathode (A_{fc}) were 0.041 cm and 0.36 cm^2, respectively. Figure 3 shows Sherwood number as a function of Reynolds number. Following Landolt [21], some theoretical relations for laminar and turbulent flow are included. For laminar flow it concerns [21, 25, 26, 29]:

$$Sh = 1.85 \times \left[\frac{(Re\, Sc\, D_h)}{L}\right]^{1/3} \tag{2}$$

In this equation the entrance effect of the mass transfer profile is taken into account. Equation 2 only holds for the case of a fully developed velocity profile, which is roughly fulfilled in our cell. Nevertheless, the calculated *Sh* numbers are larger than the experimental for $100 < Re > 2500$. Moreover, the slope of the experimental curve is somewhat smaller (∼0.27) than the 0.33, predicted by Equation 2. This in contrast to the results of Landolt, who obtained a very good agreement between experimental data and Equation 2.

To fit data for turbulent flow, Landolt used the equation [4, 21, 26, 27, 29]:

$$Sh = 0.022\, Re^{7/8}\, Sc^{1/4} \tag{3}$$

Equation 3 holds for fully developed velocity and temperature or mass transfer profiles. However, it is questionable whether fully developed mass transfer is reached in the main part of the electrode [4]. Although [25], the mass transfer entry region is much shorter in turbulent flow than in laminar flow, the results obtained by Shaw, Reiss and Hanratty indicate that this entry length ranges from about 2 to 0.5 diameters as the Reynolds number increases from 5000 to 75 000 [28]. For turbulent pipe flow with fully developed velocity profile, the mass transfer rate in the entry region is given by [28–30]:

$$\langle Sh \rangle = 0.28\, Re^{0.58}\, Sc^{1/3}\, (D/x)^{1/3} \tag{4}$$

As can be seen from Figure 3, the calculated Sherwood numbers are larger than the experimental values, and moreover, the slope of the experimental curve (∼0.70) is smaller than that predicted by Equation 3. Using Equation 4 results in Sherwood numbers which are larger than the experimental values. However, the slope of the experimental curve is slightly larger than that predicted by Equation 4. Landolt found good agreement between experiment and theory using Equation 3 [21].

Although the experimental Sherwood numbers are smaller than the values expected based from relationships for laminar and turbulent flow and, moreover, discrepancies between theoretical and experimental slopes exist, a transition is visible at $Re \approx 2500$ ($V = 500$ cm s^{-1}), most probably associated with transition from laminar to (partly developed) turbulent flow.

The origin of the difference between the experimental Sherwood numbers and values calculated by Equations 2, 3 and 4 is not clear. Some attempts to explain it by, for example, considering a possible effect of the relatively small interelectrode gap [31] failed.

The experiments discussed in the rest of this paper were performed at $V = 1500$ cm s^{-1} which corresponds to $Re \approx 5565$ ($\nu = 0.011\,05$ cm^2 s^{-1} for a solution of 230 g l^{-1} $NaNO_3$ [23]). Under these conditions, turbulent flow is expected.

2.6. *Materials*

Copper, nickel and two nickel–copper alloys (Ni30Cu70 and Ni65Cu32) were used in high-rate dissolution experiments. The composition of the materials was verified using energy dispersive spectroscopy (EDS). In the pure metals, no contaminants could be detected. The Ni30Cu70 alloy contained 30% nickel and 70% copper by weight which was confirmed by EDS. The Ni65Cu32 alloy contained in addition to nickel and copper, small amounts of iron and manganese. The composition of this material as determined by EDS was as follows: 64.6% Ni, 32.1% Cu, 1.5% Fe and 1.8% Mn. A possible effect of small amounts of Fe and Mn on the electrochemical dissolution behaviour was neglected.

2.7. *High-rate dissolution experiments*

High-rate electrochemical dissolution experiments were carried out in 230 g l^{-1} $NaNO_3$ at 25 °C and $V =$ 1500 cm s^{-1}. To determine the current efficiency curves of Ni, Cu and the alloys, dissolution experiments were carried out under current-controlled conditions at different current densities. To calculate the current density at the anode, the surface area of the machined workpiece was used which was about 0.39 cm^2 (the surface area of the cathode was 0.36 cm^2; the effective anode surface was somewhat larger due to stray currents). For each point in the current efficiency curve, a new metal sample was used. Anodic current densities ranged from 8 to 132 A cm^{-2}. Per sample, 60 C of charge was supplied using direct current. After the dissolution experiment, the weight loss, Δm, of the sample was measured using a Mettler AT261 Delta Range balance. To determine the current efficiency θ (%), the following equation was used:

$$\theta = \frac{F\Delta m}{60} \times 100 \times \sum_i \frac{x_i n_i}{M_i} \qquad (5)$$

The voltammograms were measured in the following way. At an initial gap of $h = 208$ μm, a given current was switched-on, and anode dissolution was performed for a time corresponding to passing a charge of 60 C. During this time, the variation of the cell voltage (U) between the electrodes was recorded and used for calculation of U at a given j. This voltage U is the sum of the anodic and cathodic potentials $E_a + E_c (= E_{el})$ and the ohmic voltage drop in the interelectrode gap (U_{ohm}). Ignoring the effects of the products of electrochemical and chemical reactions and variation of the temperature in the gap, U_{ohm} was calculated from the reference value of the conductivity of the $NaNO_3$ solution. In the analysis of the voltage balance, we used available data of anodic and cathodic potentials.

We took into account that the Ni–Cu alloys were single-phase homogeneous solid solutions and assumed that the oxidation state of nickel, copper and iron was two, and the oxidation state of Mn was four.

3. Results and discussion

Upon switching-on the current, the electrolyte temperature increased, first, steeply for about 0.25 s and, then, very slowly up to 15 °C depending on j, as a result of the Joule effect. A high current passing through a narrow gap caused not only heating, but also a very small decrease in the volume flow of electrolyte (for example 1.89 to 1.85 l min^{-1}), possibly associated with the formation of the electrolysis products in the gap. We observed also a small increase of the electrolyte bulk pH (by 0.1–0.3) at the gap outlet.

3.1. *Current efficiency measurements*

Figure 4 gives the current efficiency θ of metal dissolution against current density j. For nickel dissolution, θ increases with j, starting from low values and reaching a value slightly higher than 90%. This is in agreement with earlier results (see Section 1). For anodic copper dissolution, θ is close to 100% for low j, and the apparent magnitude of θ increases for j above a certain value (about 40 A cm^{-2}). The excess of 100% apparent current efficiency is associated with the reported decrease in the copper oxidation state for dissolution at $j > j_{cr}$ [5, 8].

At low j, the behaviour of the current efficiency for both Ni–Cu alloys is similar to that of copper: high θ

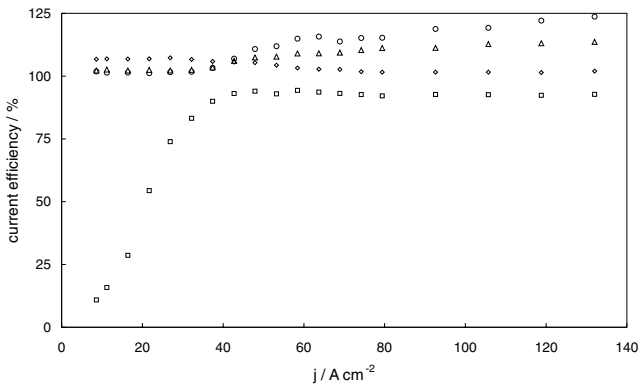

Fig. 4. Dependence of the current efficiency of (○) copper, (□) nickel, (△) Ni30Cu70, and (◇) Ni65Cu32 anodic dissolution on the current density.

values slightly exceeding 100% were obtained. For j higher than about 40 A cm^{-2}, the current efficiency for the dissolution of the alloy with a relatively high copper content increases. This increase is somewhat smaller than for pure copper. For the alloy less rich in copper, the effect of nickel is more pronounced. Overall, Figure 4 shows the predominant effect of copper on the anodic behaviour of the alloys.

In addition, the results presented in Figure 4 lead to one practically important conclusion: the accuracy of ECM parts made of copper–nickel alloys with a nickel content up to at least 65% in sodium nitrate will be essentially lower than for nickel due to the absence of an increase of θ with increasing j, which is typical for nickel.

3.2. *Surface brightening*

Figure 5 gives the dependence of the percentage of surface area of nickel, copper and the two nickel–copper alloy anodes appearing bright on applied current density. It was found that for these materials brightening started at $j \approx 40$ A cm^{-2} downstream and propagated over the specimen surface with increasing j. The dependence of the percentage of surface area of the nickel anode appearing bright on j is similar to that reported [11]. Figure 5 shows that in the current density range from about 40 to 70 A cm^{-2}, a transition from entire surface etching to brightening of more than 80% of the surface occurs. For copper, the start of surface brightening coincides with the transition from active to transpassive dissolution (see Section 1 and Figure 4). It should be noted that the maximum percentage of brightening of the alloys is somewhat higher than that of both pure metals.

3.3. *Voltage transients*

In Figure 6 schematic drawings of two types of cell voltage transients obtained in this study are presented. Figure 6(a) corresponds to transients obtained at $j < j_{cr}$ and Figure 6(b) corresponds to transients obtained at $j > j_{cr}$. Upon switching-on $j < j_{cr} \approx j_l$ (about j_{cr} and j_l see Section 1), the cell voltage abruptly increases (Figure 6(a)) to a value U_i corresponding to metal dissolution in absence of mass transfer limitation. The dissolution product concentration near the electrode surface increases as current passes, but cannot reach saturation at $j < j_{cr}$. Subsequently, U slowly increases linearly because the gap increases as metal dissolves. Extrapolation of the linear segment of the cell voltage transient to $t = 0$ yields a voltage ($U_{i,ext}$) required for metal dissolution at a given j for $h = 208$ μm. In Figure 7 the measured cell voltage transients obtained for nickel, copper and the two nickel–copper alloys at $j = 8.6$ A cm^{-2} are presented ($j < j_{cr}$).

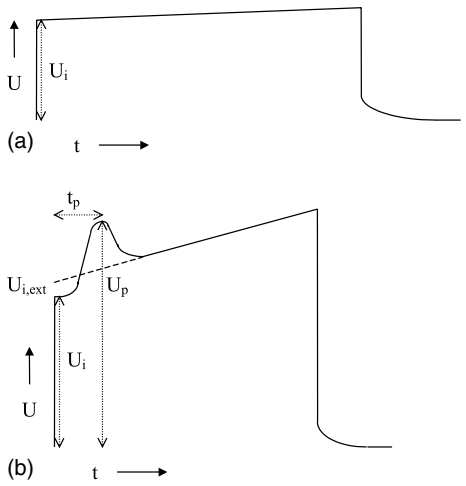

Fig. 6. Schematic drawing of two types of cell voltage transients: (a) $j < j_l$, (b) $j > j_l$.

For $j > j_{cr}$ (Figure 6(b)), a voltage delay is observed corresponding to metal dissolution in the same voltage range as in Figures 6(a) and 7. An increase in the concentration of the dissolution products at $j > j_{cr}$ may lead to saturation of the solution in the near-electrode layer (even super-saturation may occur for a short time). Reaching this stage takes a certain time, after which a solid dissolution product (a salt of the dissolved metal) is deposited on the electrode. This results in an increase in the system resistance, as can be seen from the abrupt

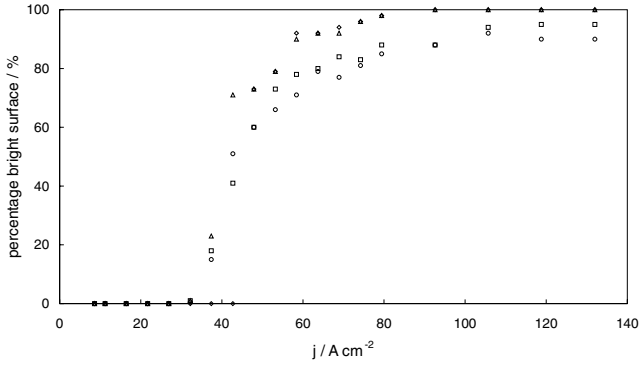

Fig. 5. Dependence of the percentage of surface area of (○) copper, (□) nickel, (△) Ni30Cu70, and (◇) Ni65Cu32 anodes appearing bright on the current density.

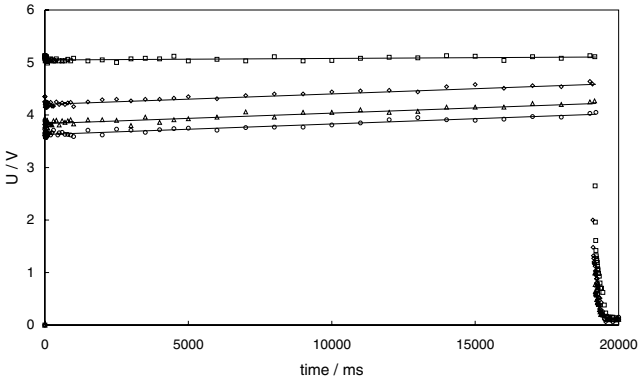

Fig. 7. Cell voltage transients measured at $j = 8.6$ A cm^{-2} in sodium nitrate for (○) copper, (□) nickel, (△) Ni30Cu70, and (◇) Ni65Cu32.

increase in U (Figure 6(b)). After passing through a maximum (U_p), U decreases to a certain value depending on the metal nature and corresponds to dissolution in the overlimiting current region (Section 1). This decrease of U with time, is probably caused by salt film dissolution in the transition from the limiting current region to overlimiting current region. Then U starts to increase again slowly because the interelectrode distance increases during anode dissolution. It may be assumed that, in the transition from the limiting to overlimiting current region, a thick salt film preventing current increase with potential in the limiting current region (Figure 1, 'bc' or 'fg') is substituted by another, significantly thinner, film which does not prevent an increase in current with potential, but suppresses etching and assists formation of a bright anode surface. This film does not thicken significantly with an increase of E_a nor does it possesses high resistance this is indicated by the large slope of the polarization curve in region 'cd' or 'gi' in Figure 1. Unfortunately, the mechanism of metal dissolution in the overlimiting current region is not well understood. By extrapolating the linear segments of the anodic transients to $t = 0$ (Figure 6(b)), we can obtain $U_{i,ext}$, required for metal dissolution at a given j for $h = 208$ μm, in the same way as for $j < j_{cr}$.

Figure 8 shows experimental cell voltage transients for nickel, copper and the two nickel–copper alloys obtained at $j = 58.4$ A cm^{-2}. From Figure 8(a) (overview) the linear relationship between U and time in the overlimiting current density region is clearly visible. Figure 8(b) shows some details of the transients during the nonsteady state period. This figure shows that U_p is not as well determined as suggested in the schematic drawing presented in Figure 6(b); in many cases, in addition to the main peak (with a maximum U_p), one or two smaller peaks were also found.

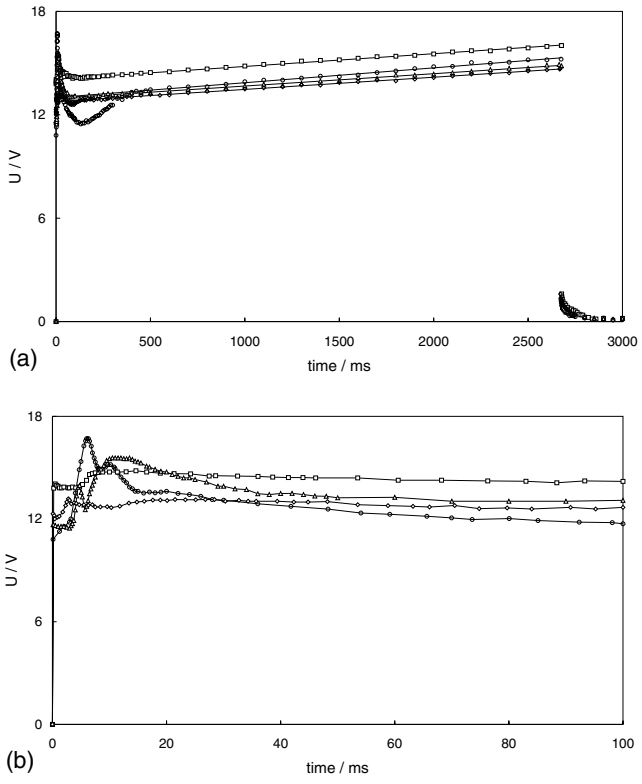

Fig. 8. Cell voltage transients measured at $j = 58.4$ A cm^{-2} in sodium nitrate for various materials (for composition see Figure 7): (a) total transient and (b) initial segment.

From the voltage transients two additional Figures were constructed. In Figure 9 the difference between U_p and U_i is presented as a function of j. In Figure 10 $U_{i,ext}$ is given as a function of j.

Concerning Figure 9, similar figures (E_a as a function of j, U as a function of j or $U_p - U_i$ as a function of j) have been reported for copper [4, 5] as well as nickel [11, 14, 32–34]. A large variation in $U_p - U_i$ values was found for both Cu and Ni. $U_p - U_i$ depends on parameters such as electrolyte velocity, concentration, temperature, pH, pulse-on time and pulse-off time. These parameters affect the current density where mass transfer controlled dissolution starts, as well as the magnitude of the voltage increase. A lower flow rate, higher concentration, lower temperature, longer pulse-on times and shorter pulse-off times promote the change to mass transfer controlled dissolution and, at the same j, a relatively large voltage increase. The sensitivity of mass transfer controlled dissolution to so many process parameters makes it very difficult to compare the behaviour of copper and nickel based on literature results.

Although there is considerable scatter in the data points presented in Figure 9, it is clear that the nonsteady state behaviour of the copper-rich alloy during the transition to the limiting and overlimiting current regions strongly resembles the behaviour of copper. By contrast, the nickel-rich alloy behaves like nickel. Except for copper, the appearance of a peak in the cell voltage transients at $j \approx 40$ A cm^{-2} corresponds to the (visual) start of surface brightening.

During high-rate anodic dissolution of nickel in 230 g l^{-1} $NaNO_3$ at very small interelectrode distances and a high flow velocity, for $j > j_{cr}$, extrapolation of the

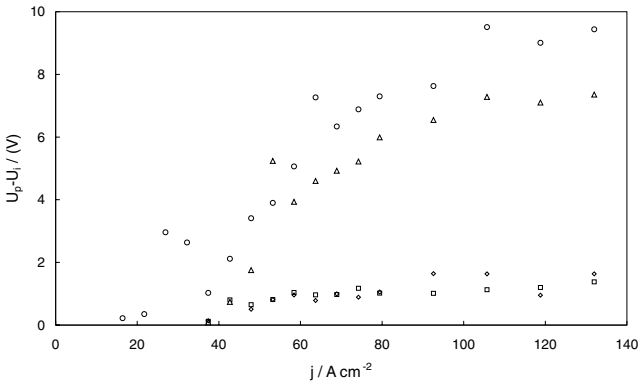

Fig. 9. Dependence of the difference between peak voltage U_p and voltage U_i obtained immediately after switching-on the current on the current density for (○) copper, (□) nickel, (△) Ni30Cu70, and (◇) Ni65Cu32.

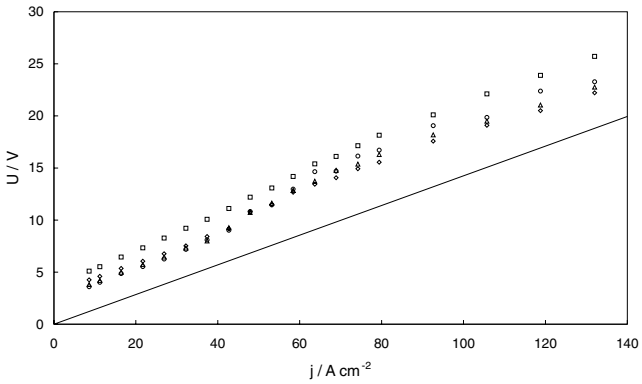

Fig. 10. Experimental voltammograms ($U_{i,ext}/j$) of (○) copper, (□) nickel, (△) Ni30Cu70, and (◇) Ni65Cu32, and the calculated curve of the ohmic voltage drop in the interelectrode gap of 208 μm filled with $NaNO_3$ solution of concentration 230 g l^{-1} (straight line).

linear segment of the cell voltage transient to $t = 0$ yields voltages ($U_{i,ext}$) almost equal to the voltage obtained immediately after switching-on the current (U_i), prior to the voltage peak caused by the transition to limiting and overlimiting currents. Under these conditions, the limiting-current plateau in the voltammogram will be virtually absent (Figure 10), though the transition to overlimiting currents exists. The latter is indicated both by the peak in the cell voltage transient (Figures 8 and 9) and by a typical change in the metal surface appearance (Figure 5). The voltammogram for nickel obtained in this work corresponds to a portion of the total polarization curve between the potential of the onset of oxygen evolution (E_{ox}) and point '*i*', Figure 1. The complete polarization curve has been reported elsewhere [11, 15]. The difference is that in our results (Figure 10) no clear limiting current region 'fg' is observed (Figure 1), though transition from $j < j_{cr}$ to $j > j_{cr}$ takes place. This can be explained by the fact that during high-rate anodic metal dissolution, the potential range of the limiting current plateau decreases with increasing electrolyte flow [8, 11, 17]. For nickel dissolution in $NaNO_3$ at relatively low velocities, this plateau is observed [11, 15] and occupies a small potential range, but at a high flow it virtually vanishes.

During anodic copper dissolution in $NaNO_3$, the limiting current plateau usually occupies a significantly wider potential range than in the case of nickel [4, 5]. Therefore, in our experiments, at very small interelectrode distance and high velocity, for copper dissolution an ill-defined limiting current plateau is observed at $j \approx 50$ A cm^{-2} (Figure 10), which is smaller than in [4, 5]. The cell voltage prior to reaching j_l is lower than for nickel, in agreement with available data [8, 9, 15]. However, under our conditions, high-rate copper dissolution in the transpassive state also requires a lower voltage than for nickel dissolution because of the narrow limiting current plateau.

Figure 10 also gives voltammograms for both nickel–copper alloys and U_{ohm}, calculated for $h = 208$ μm (according to [23], p. D-258 for a solution of 230 g l^{-1} $NaNO_3$ $\sigma = 134$ mS cm^{-1} at 20 °C, which results, after temperature correction, in $\sigma \approx 146$ mS cm^{-1} at 25 °C). Figure 10 shows that the voltammograms for the alloys lie significantly closer to the curve for copper than to that for nickel. This is in agreement with results obtained at low j in corrosion studies, [17, 18]. In these studies it was shown that the polarization curves for nickel–copper alloys in acidic solution lie in the region of pure copper dissolution. According to these data, the dissolution rate of the alloys with 30 and even 65% nickel is controlled, to a large extent, by the copper component, that is, nickel dissolves from the alloy at less positive potentials than pure nickel does under similar conditions. This means that a small amount of copper in the alloy prevents nickel passivation. Earlier, a similar result was obtained for high-rate dissolution of nickel–chromium alloys in chloride electrolyte: the presence of nickel in the alloy prevented chromium passivation [3].

Comparing the results presented in Figures 10 and 5, we see that the limiting current plateau in the voltammogram coincides with the onset of brightening, in agreement with data reported before [11].

As was mentioned before, at a given j, $U_{i,ext}$ is the algebraic sum of the anodic (E_a) and cathodic (E_c) potentials (E_{el}) and U_{ohm} for $h = 208$ μm. Subtracting U_{ohm} from $U_{i,ext}$ at a given j, we obtain an approximate magnitude of E_{el}, neglecting variations in the conductivity of the electrolyte in gap due to a gas fraction and Joule heating. Potential measurements at high j are difficult, resulting in discrepancies between electrode potentials reported by different authors [10, 35, 36]. Therefore, we can discuss only approximate values of the components of the voltage balance.

For example, for nickel at $j = 40$ A cm^{-2}, $U_{i,ext}$=10.5 V (Figure 10). Taking into account $\sigma = 146$ mS cm^{-1}, U_{ohm} at 40 A cm^{-2} is 5.7 V. According to [9], at this current density the potential of a stainless steel cathode in a $NaNO_3$ solution is −1.4 V and the nickel electrode potential is 2.22 V [10]. This results in $E_{el} = 3.62$ V. All electrode potentials are given with respect to the standard hydrogen electrode. The sum of E_{el} and U_{ohm} is 9.32 V. Consequently, the difference between this value and $U_{i,ext}$ is approximately one volt. On first sight this difference may be ascribed to the effect of gas evolution, but results of Landolt et al. [37], under more or less similar conditions indicated that the effect of gas bubbles on U_{ohm} was very small at high electrolyte flow rates.

A similar calculation may by performed for high-rate copper dissolution. Assuming that the cathode potential in a $NaNO_3$ solution and U_{ohm} at a given j are independent of the anode material, we obtain, for $j =$ 40 A cm^{-2}, $E_c + E_a + U_{ohm} = 1.4 + 0.54 + 5.7 = 7.64$ V, where $E_a = 0.54$ V was calculated from results from [38]. From Figure 9 we obtain $U_{i,ext} = 8.5$ V for copper, that is, a difference of about 1 V.

Similar calculations can be performed for the alloys. It should be noted that, in principle, calculations can

also be performed in the overlimiting current region, but nothing is known about the dependence of E_a and E_c on j and about U_{ohm} in this region.

4. Conclusions

The results of the current efficiency measurements of Ni and Cu are in agreement with literature data. For $j < j_l$ the alloys behave like copper (high current efficiency), at $j > j_l$ they show intermediate behaviour. From the current efficiency curves it can be concluded that the accuracy of ECM for both nickel–copper alloys as well as for copper will be considerably lower than for nickel.

For all materials, the limiting current density j_l of anodic dissolution was reached due to formation of a salt film on the electrode. At $j < j_l$, all specimens had an etched surface, for $j > j_l$ the surface became (partly) bright. Under the experimental conditions, the limiting current plateau occupied a narrow voltage range. Subsequently, at higher voltages, the current increased further with voltage in the region of overlimiting current.

References

1. A.D. Davydov and J. Kozak, 'Vysokoskorostnoe Elektrokhimicheskoe Formoobrazovanie' (High-Rate Electrochemical Shaping), Nauka, Moscow (1990).
2. A.D. Davydov, *Electronnaya Obrabotka Materialov* **3** (1980) 18.
3. A.D. Davydov, E.N. Kiriyak and V.D. Kashcheev, *Elektrokhimiya* (Soviet Electrochemistry) **14** (1978) 420.
4. D. Landolt, R.H. Muller and C.W. Tobias, *J. Electrochem. Soc.* **116** (1969) 1384.
5. K. Kinoshita, D. Landolt, R.H. Muller and C.W. Tobias, *J. Electrochem. Soc.* **117** (1970) 1246.
6. D. Landolt, R.H. Muller and C.W. Tobias, *J. Electrochem. Soc.* **118** (1971) 40.
7. D. Landolt, R.H. Muller and C.W. Tobias, *J. Electrochem. Soc.* **118** (1971) 36.
8. A.I. Dikusar, G.S. Domente, G.R. Engel'gardt, G.N. Zaidman, V.I. Petrenko, A.N. Musiatse and A.N. Molin, *Electronnaya Obrabotka Materialov* **3** (1983) 21.
9. A.D. Davydov, R.A. Mirzoev, V.D. Kashcheev and B.N. Kabanov, *Elektrokhimiya* **8** (1972) 1500.
10. J. Hives and I. Rousar, *J. Appl. Electrochem.* **24** (1994) 798.
11. M. Datta and D. Landolt, *J. Electrochem. Soc.* **122** (1975) 1466.
12. M. Datta and D. Landolt, *J. Electrochem. Soc.* **124** (1977) 483.
13. M. Datta, H.J. Mathieu and D. Landolt, *Electrochim. Acta* **24** (1979) 843.
14. M. Datta and D. Landolt, *J. Appl. Electrochem.* **7** (1977) 247.
15. A.D. Davydov, V.D. Kashcheev and R.A. Mirzoev, *Fizika i Khimiya Obrabotki Materialov* **3** (1974) 38.
16. A.I. Dikusar, G.E. Engel'gardt, A.N. Molin, A.D. Davydov and E.A. Vysokova, *Elektronnaya Obrabotka Materialov* **1** (1987) 53.
17. A.D. Davydov, V.D. Kashcheev and R.A. Mirzoev, *Fizika i Khimiya Obrabotki Materialov* **6** (1973) 32.
18. I.A. Makhovetskaya, V.V. Skorchelletty and N.N. Ozhiganova, *Zashchita Metallov* (Metal Protection) **5** (1969) 215.
19. E.I. Zolotarev, A.P. Pchel'nikov, Ya.B. Skuratnik, M.A. Dembrovskii, N.I. Khokhlov and V.V. Losev, Ozhiganova, *Zashchita Metallov* **23** (1987) 922.
20. R.D. Misra and G.T. Burstein, *J. Electrochem. Soc.* **131** (1984) 1515.
21. D. Landolt, *Rev. Sci. Instrum.* **43** (1972) 592.
22. V.G. Levich, 'Physicochemical Hydrodynamics' (Prentice Hall, Englewood Cliffs, NJ 1962).
23. R.C. Weast, M.J. Astle and W.H. Beyer (Eds), 'CRC Handbook of Chemistry and Physics' (CRC Press, Boca Raton, FA, 69th edn, 1988), pp. D-246.
24. K.I. Darrall and J. Oldman, *J. Chem. Soc. A* (1968) 2584.
25. J. Newman, *Ind. Eng. Chem.* **60** (1968) 12.
26. J.R. Selman and C.W. Tobias, *Adv. Chem. Eng.* **10** (1978) 211.
27. R. Bird, W.E. Stewart and E.N. Lightfoot, 'Transport Phenomena' (John Wiley & Sons, New York, 1960), p. 403.
28. P.V. Shaw, L.P. Reiss and T.J. Hanratty, *A.I.Ch.E. J.* **9** (1963) 362.
29. D.J. Pickett, 'Electrochemical Reactor Design' (Elsevier, Amsterdam, 1977), pp. 121–170.
30. T.K. Ross and A.A. Wragg, *Electrochim. Acta* **10** (1965) 1093.
31. X.F. Peng and B.X. Wang, *in* G.F. Hewitt (Ed.), 'Heat Transfer 1994', Proceedings of the 10th international Heat Transfer Conference Vol. 1 (Inst. Chem. Eng., Rugby, UK, 1994), pp. 159–177.
32. M. Datta and D. Landolt, *Electrochim. Acta* **25** (1980) 1255.
33. M. Datta and D. Landolt, *Electrochim. Acta* **25** (1980) 1263.
34. M. Datta and D. Landolt, *Electrochim. Acta* **27** (1982) 385.
35. D. Landolt, *in* R.P. Frankenthal and J. Kruger (Eds), 'Passivity of Metals' (Electrochemical Society, Princeton, NY 1978), pp. 484.
36. A.D. Davydov, *Electronnaya Obrabotka Materialov* **5** (1975) 19.
37. D. Landolt, R. Acosta, R.H. Muller and C.W. Tobias, *J. Electrochem. Soc.* **117** (1970) 839.
38. R. Saubetin and D. Landolt, *J. Electrochem. Soc.* **129** (1982) 946.